

SCIENTIFIC REPORTS

OPEN

Computational measurement of tumor immune microenvironment in gastric adenocarcinomas

Young Hwan Chang¹, You Jeong Heo², Junhun Cho³, Sang Yong Song³, Jeeyun Lee⁴ & Kyoung-Mee Kim³

Received: 20 June 2018

Accepted: 5 September 2018

Published online: 17 September 2018

The use of four groups of tumor immune microenvironments (TME) based on PD-L1 and tumor-infiltrating T lymphocytes (TIL) is a reliable biomarker for anti-PD-1/PD-L1 inhibitor therapy. We classified the TME in 241 gastric cancers which were subdivided according to 40 EBV+, 76 microsatellite instability-high (MSI-H), and 125 EBV-/microsatellite-stable (MSS) subtypes by quantitative image analysis (QIA) and correlated the results with mRNA expression levels. The mean PD-L1 ratio and CD8 ratio in EBV+, MSI-H, and EBV-/MSS GCs were significantly different ($P < 0.006$). The PD-L1 ratio and CD8 ratio obtained by QIA correlated well with the RNA levels of PD-L1 ($r = 0.63$) and CD8 ($r = 0.67$), respectively. The TME were type I (PD-L1^H/CD8^H) in 45, type II (PD-L1^L/CD8^L) in 106, type III (PD-L1^H/CD8^L) in 8, and type IV (PD-L1^L/CD8^H) in 82 cases. The type I TME was significantly associated with high TIL ($P = 3.0E-11$) and EBV+ status ($P = 8.55E-08$). In conclusion, QIA results correlated well with the mRNA expression levels and classified TME of gastric cancers.

Precision cancer treatment depends not only on next-generation sequencing (NGS), but also on visual assessment of protein biomarker expression seen on immunohistochemistry (IHC) slides. Pathologists interpret IHC results, a difficult and time-consuming task. However, the final IHC results are subjective and qualitative in nature. There is inter-observer variability, and this method is not well suited to the evolving landscape of biomedical research¹. This variability among pathologists, coupled with the inherent heterogeneity seen among cancers, suggests that a more objective and truly quantitative strategy is the true gold standard toward which the biomedical community should strive². Therefore, the advent of high-throughput acquisition technologies, such as automated slide scanners and computerized analysis of tissue images, is highly desirable. Studies have shown that quantitative software can detect changes in disease states that are missed by visual inspection³.

The tumor immune microenvironment (TME) is increasingly recognized as a key factor in multiple stages of disease progression, particularly local resistance, immune-escaping, and distant metastasis. The TME substantially impacts the future development of frontline interventions in clinical oncology⁴. The use of four TME groups based on PD-L1 and tumor-infiltrating lymphocytes (TIL) status is a reliable biomarker for anti-PD-1/PD-L1 inhibitor therapy. Immunohistochemistry (IHC) is currently used to detect PD-L1 on tumor cells and immune cells. However, positivity and clinical significance vary due to the type of specimen used (whole histological sections vs. tissue microarrays), type of PD-L1 primary antibodies, and pathological interpretation method⁵⁻⁷. The addition of immune cellular markers to PD-L1 IHC would provide deeper insight into the understanding of the complex TME⁸.

Recently, immunotherapy has become a promising approach to treat GC⁹. We hypothesized that if a full-section quantitative image analysis (QIA) method can classify TME subtypes, it can be used as a predictive biomarker for anti-PD-1/PD-L1 inhibitor therapy with high reproducibility. For this purpose, we performed IHC for PD-L1 and CD8+ T cells in three distinct subtypes of gastric cancer (GC) (EBV+, MSI-H, and EBV-/MSS), interpreted them with QIA and correlated the results with mRNA expression levels.

¹Department of Biomedical Engineering and Computational Biology Program, Oregon Health and Science University (OHSU), Portland, OR, 97239, USA. ²The Samsung Advanced Institute for Health Sciences & Technology (SAIHST), Samsung Medical Center, Sungkyunkwan University School of Medicine, Seoul, Korea. ³Department of Pathology & Translational Genomics, Samsung Medical Center, Sungkyunkwan University School of Medicine, Seoul, Korea. ⁴Division of Hematology-Oncology, Department of Medicine, Samsung Medical Center, Sungkyunkwan University School of Medicine, Seoul, Korea. Young Hwan Chang, You Jeong Heo and Junhun Cho contributed equally. Correspondence and requests for materials should be addressed to K.-M.K. (email: kkmkys@skku.edu)

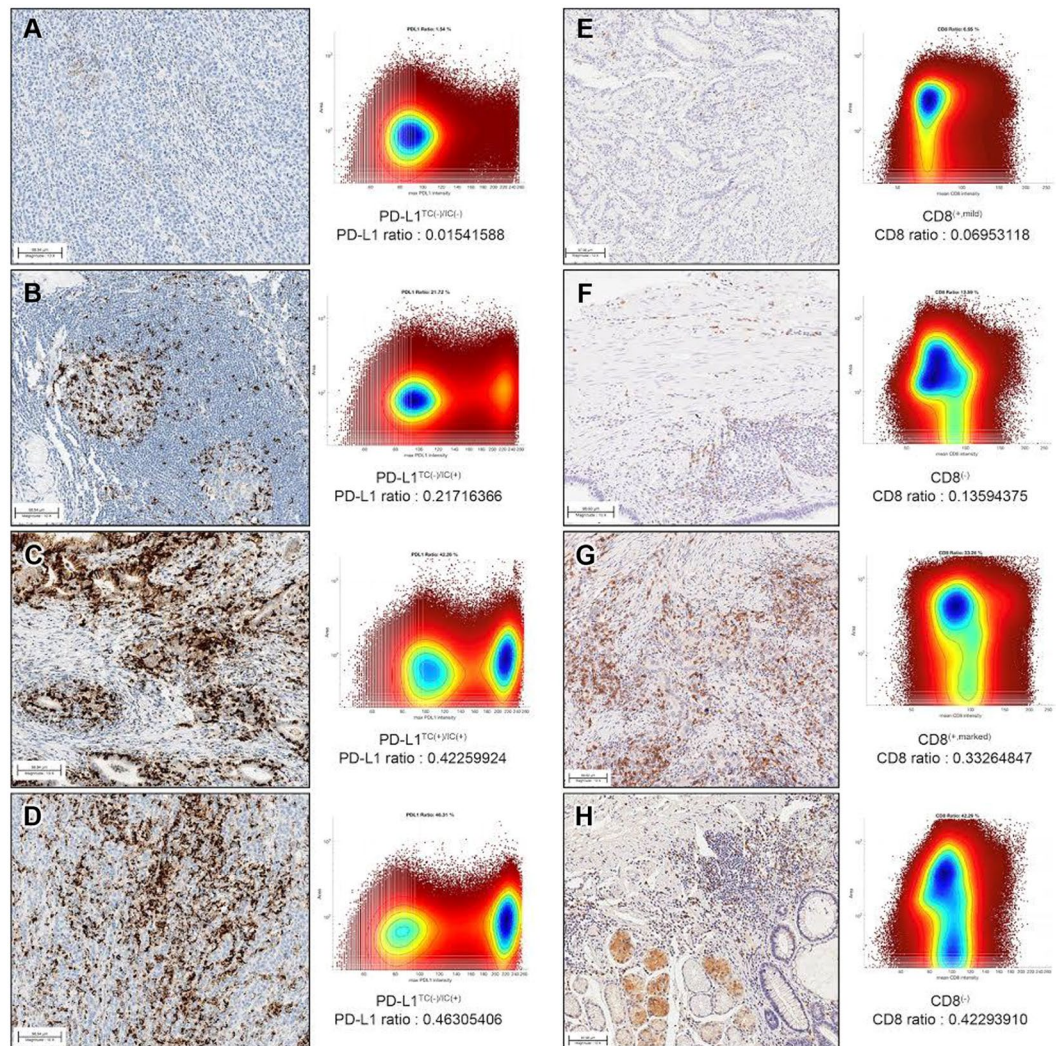


Figure 1. Representative images of PD-L1 (A–D) and CD8 (E–H) immunohistochemistry. PD-L1 ratio (A–D) and CD8 ratio (E–H) were obtained from computational analyses.

Results

Quantitative image analyses (QIA) of PD-L1 and CD8 IHC. In QIA of whole slide imaging, representative images of PD-L1 (Fig. 1A–D) and CD8 (Fig. 1E–H) IHC, with paired bivariate scatter plots for both cell size (area) and intensity values, are provided in Fig. 1, where each dot represents a single cell. In the representative whole IHC-stained slides from each GC case, the mean number of PD-L1-positive cells was 206,132 (range: 12,415–696,449), and the mean number of total cells on a slide was 1,555,897 (range: 26,065–2,821,182). The mean PD-L1-ratio (absolute number of PD-L1-positive cells per total number of cells) was 0.1387 (range: 0.0154–0.4763). The mean number of CD8-positive cells was 532,128 (range: 142,374–1,716,791), and the mean number of total cells within the slide was 2,197,705 (range: 622,033–4,388,177). The mean CD8 ratio was 0.2332 (range: 0.0695–0.4876).

The QIA results regarding PD-L1 ratio, PD-L1 count, CD8 ratio, and CD8 count in 40 EBV+, 76 MSI-H, and 125 EBV(-)/MSS GCs are described in Table 1. The mean (standard deviation: SD) PD-L1 ratios in EBV+, MSI-H, and EBV-/MSS GCs were 0.19 (0.13), 0.10 (0.08), and 0.06 (0.06), respectively, and this difference was significantly different ($P < 0.001$). The mean (SD) CD8 ratios in EBV+, MSI-H, and EBV-/MSS GC were 0.25 (0.14), 0.21 (0.12), and 0.18 (0.11), and these differences were significant ($P = 0.006$).

Interestingly, although the PD-L1 ratio and count were significantly higher in both the EBV+ and MSI-H GC groups, the CD8 ratio and CD8 count were significantly higher in the EBV+ GC group, but not in the MSI-H GC group, compared to the MSS GC group. This result suggests that CD8+ cells heavily infiltrate both EBV+ and MSI-H GC, but there is a lower degree of infiltration in MSI-H GC compared to EBV+ GC.

Comparison of QIA to mRNA expression and clinicopathological variables. Direct comparison of mRNA expression levels and QIA results showed a higher correlation between PD-L1 mRNA expression level and PD-L1 ratio ($r = 0.63$) than with PD-L1 count ($r = 0.22$). CD8 mRNA was more highly correlated with CD8 ratio ($r = 0.67$) than CD8 count ($r = 0.34$) (Fig. 2).

	EBV+	MSI-H	EBV-/MSS	p value
QIA mean values (standard deviation)				
PD-L1 ratio	0.19 (0.13)	0.10 (0.08)	0.06 (0.06)	<0.001
PD-L1 counts	308789.22 (262974.48)	142755.72 (124169.97)	92239.30 (100996.94)	<0.001
CD8 ratio	0.25 (0.14)	0.21 (0.12)	0.18 (0.11)	0.006
CD8 counts	382905.08 (272642.21)	268919.76 (192954.09)	240017.42 (208248.02)	0.002
Number of cases	40	76	125	

Table 1. Results of quantitative image analysis in three distinct subtypes of gastric carcinomas.

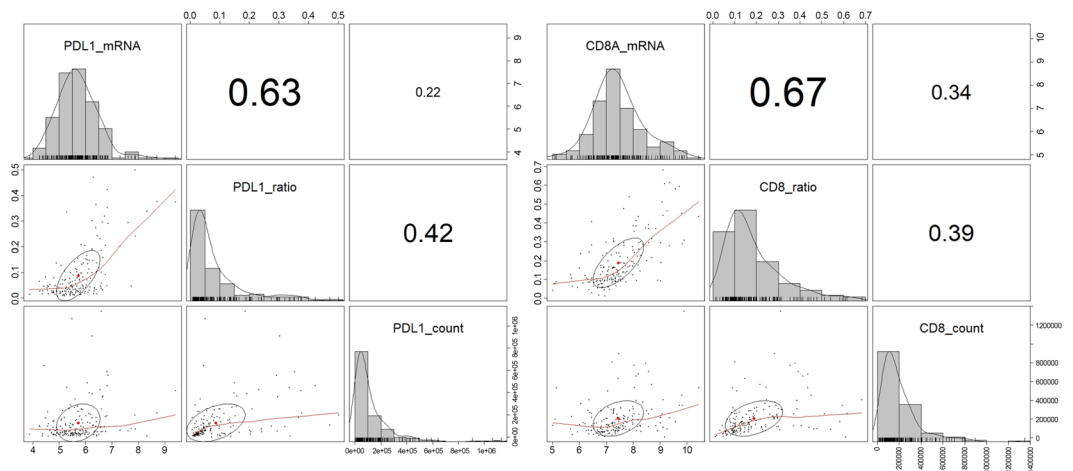


Figure 2. Direct comparison of mRNA expression level and quantitative image analysis results. PD-L1 ratio showed higher correlation with PD-L1 mRNA than PD-L1 count, and CD8 ratio had higher correlation with CD8 mRNA than CD8 count.

Because there was higher correlation between PD-L1 ratio and mRNA level, PD-L1 ratio was used for comparison with clinicopathological variables. PD-L1 ratio correlated most significantly with CD8 ratio (correlation coefficient, $r = 0.60$), followed by CD8 count ($r = 0.54$), EBV status, and host inflammatory response ($r = 0.46$) (Fig. 3).

Tumor microenvironment subtypes by PD-L1 and CD8 QIA. Because PD-L1 and CD8 ratios by QIA showed high correlation with PD-L1 combined positive score (CPS) and significant survival effects compared to IHC-positive cell counts, we used PD-L1 ratio and CD8 ratio in further analyses. A cut-off value was set with the Maxstat package to divide PD-L1 and CD8 ratio status into two groups: high and low¹⁰. Of all 241 patients, the high PD-L1 ratio (PD-L1 ratio > 0.136441 ; PD-L1^H) group was comprised of 53 cases, and the low PD-L1 ratio (PD-L1^L, ≤ 0.136441) group was composed of 188 cases. A CD8 ratio of > 0.1636454 was defined as CD8-high (CD8^H), and 127 patients were identified as CD8^H. There were 30 (69.8%), 54 (68.4%), and 28 (22.4%) PD-L1^H cases of EBV+, MSI-H, and EBV-/MSS GC, respectively.

In survival analyses, EBV+ status ($P = 0.007$) was significantly associated with longer overall survival (OS), while EBV+ ($P = 0.0025$) and MSI-H ($P < 0.001$) status were significantly associated with longer disease-free survival (DFS) in univariate analysis (Supplementary Fig. 1). However, these survival differences lost their significance in multivariable Cox regression analyses, except for AJCC stage ($P < 0.001$). Forest plots of the hazard ratio (HR) for OS and DFS are described in Fig. 4.

Based on previously reported melanoma cases¹¹ and our previous observations in GC¹², TME subtypes were classified based on the QIA results of PD-L1-ratio and CD8-ratio. The TME was classified as type I (PD-L1^H/CD8^H) in 45 (18.7%) cases, type II (PD-L1^L/CD8^L) in 106 (44.0%) cases, type III (PD-L1^H/CD8^L) in 8 (3.3%) cases, and type IV (PD-L1^L/CD8^H) in 82 (34.0%) cases. The clinicopathological characteristics of the four TME types are summarized in Table 2. Pie charts of TME subtypes based on PD-L1 ratio and CD8 ratio by QIA analyses in each subtype of GC are depicted in Fig. 5A. Figure 5B shows the PD-L1 and CD8 ratios in three distinct subtypes of GC in relation to host inflammatory responses.

TME type I was most significantly associated with LELC and CLR histology ($P = 3.0E-11$) and EBV+ status ($P = 8.55E-08$). We also found that TME type IV included 10 cases with LELC histology consisting of two EBV+, five MSI-H, and three EBV-/MSS GC cases. Although EBV+ GC cases were mostly present in type I TME, it is noteworthy that MSI-H GC cases were somewhat scattered throughout diverse TME subtypes; 17.1% were type I, 42.1% were type II, 4% were type III, and 36.8% were type IV. In survival analyses, patients with type I TME showed a longer OS compared to patients with type IV TME ($P = 0.0294$).

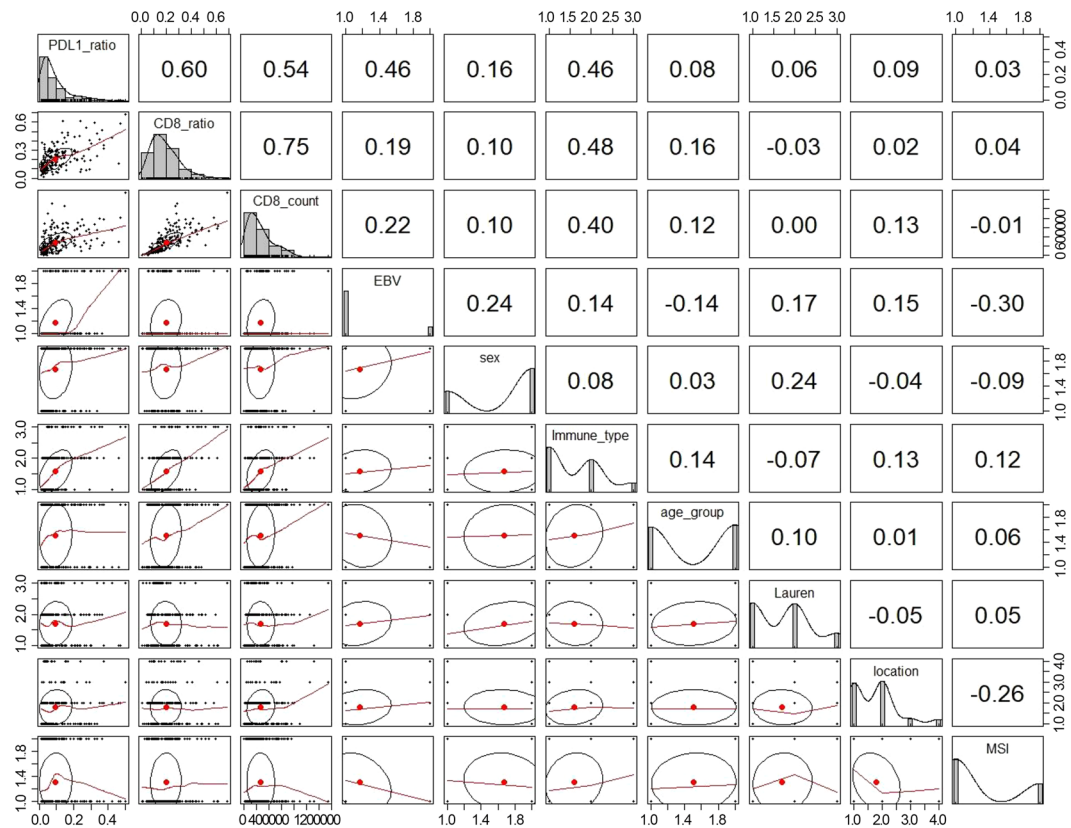


Figure 3. Correlations between PD-L1 ratio and clinicopathologic variables.

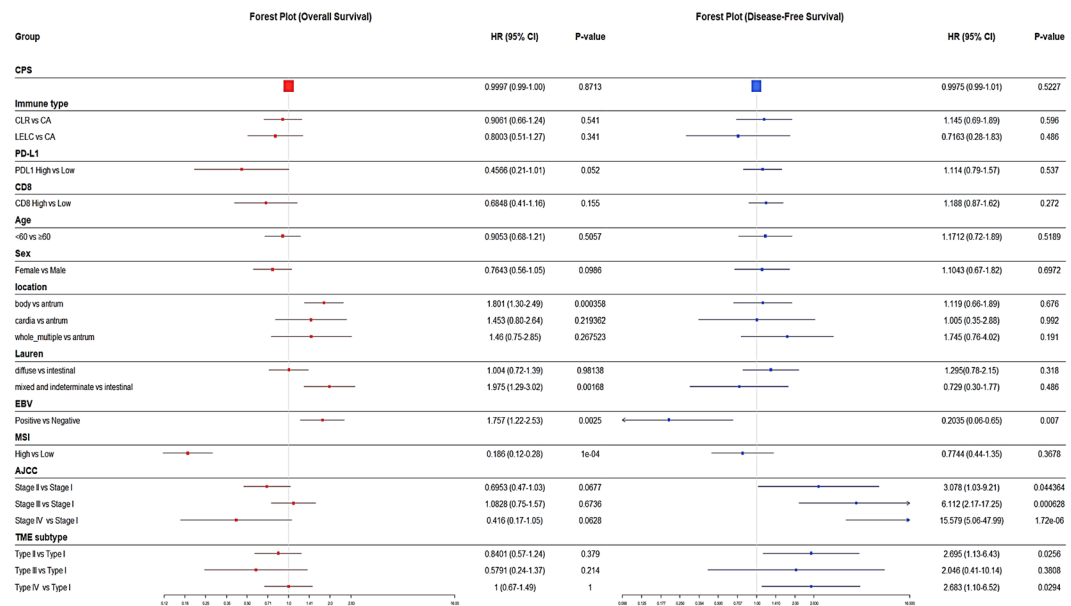


Figure 4. Forest plot of hazard ratio (HR) for disease-free survival and overall survival.

Discussion

In this study, we examined archived tumor specimens obtained from a large cohort of patients with stage IB-IV GC for IHC expression of PD-L1 and CD8 in three distinct subtypes of GC (EBV+/MSI-H/EBV- and MSS) by QIA, and correlated them with mRNA expression level and manual interpretation. Both PD-L1 ratio and CD8 ratio correlated well with their respective mRNA levels and manual interpretation results. The PD-L1 ratio

Parameters	Type I (PD-L1 ^H /CD8 ^H)	Type II (PD-L1 ^L /CD8 ^L)	Type III (PD-L1 ^H /CD8 ^L)	Type IV (PD-L1 ^L /CD8 ^H)	p value
Tumor microenvironment subtypes					
	(n = 45)	(n = 106)	(n = 8)	(n = 82)	
age					0.5269
<60	18 (40.0%)	54 (50.9%)	5 (62.5%)	41 (50.0%)	
≥60	27 (60.0%)	52 (49.1%)	3 (37.5%)	41 (50.0%)	
sex					0.2267
male	36 (80.0%)	68 (64.2%)	5 (62.5%)	52 (63.4%)	
female	9 (20.0%)	38 (35.8%)	3 (37.5%)	30 (36.6%)	
location					0.1231
cardia	7 (15.6%)	6 (5.7%)	1 (12.5%)	4 (4.9%)	
body	20 (44.4%)	50 (47.2%)	2 (25.0%)	33 (40.2%)	
antrum	15 (33.3%)	45 (42.5%)	3 (37.5%)	39 (47.6%)	
whole/multiple	3 (6.7%)	5 (4.7%)	2 (25.0%)	6 (7.3%)	
histologic type by Lauren					0.8596
intestinal	18 (40%)	44 (41.5%)	4 (50.0%)	37 (45.1%)	
diffuse	21 (46.7%)	44 (41.5%)	3 (37.5%)	36 (43.9%)	
mixed/indeterminate	6 (13.3%)	18 (17.0%)	1 (12.5%)	9 (11.0%)	
histologic type by host inflammatory response					3.06E-11
Conventional	6 (13.3%)	76 (71.7%)	3 (37.5%)	40 (48.8%)	
Crohn-like	25 (55.6%)	28 (26.4%)	5 (62.5%)	32 (39.0%)	
Lymphoepithelioma-like	14 (31.1%)	2 (1.9%)	0 (0.0%)	10 (12.2%)	
EBV					8.55E-08
Positive	20 (44.4%)	8 (7.5%)	3 (37.5%)	9 (11.0%)	
Negative	25 (55.6%)	98 (92.5%)	5 (62.5%)	73 (89.0%)	
Microsatellite instability-High					0.8911
Yes	13 (28.9%)	32 (30.2%)	3 (37.5%)	28 (34.1%)	
No	32 (71.1%)	74 (69.8%)	5 (62.5%)	54 (65.9%)	
AJCC/TNM stage					0.3979
I	12 (26.7%)	23 (21.7%)	1 (12.5%)	16 (19.5%)	
II	14 (31.1%)	31 (29.2%)	2 (25.0%)	31 (37.8%)	
III	19 (42.2%)	44 (41.5%)	3 (37.5%)	27 (32.9%)	
IV	0 (0.0%)	8 (7.5%)	2 (25.0%)	8 (9.8%)	

Table 2. Clinicopathologic parameters in four tumor microenvironment subtypes.

correlated well with CD8+ immune cells and TME subtype by QIA, and also correlated well with host inflammatory response and EBV+ GC.

Therapies blocking the PD1/PD-L1 axis have resulted in different rates of tumor response for a variety of cancer types¹³. In GC, ~50% of EBV+ and ~60% of MSI subgroups show high levels of PD-L1 expression, highlighting the molecularly defined patient population most likely to derive benefit from immune checkpoint blockade^{14–16}. Recent meta-analyses have shown GCs with high PD-L1 expression had deeper tumor infiltration (pT) and were more positive for lymph node metastasis (pN), suggesting that PD-L1 is expressed through oncogenic stimulation and is associated with poorer prognosis^{11,12,17}. Given that high PD-L1 expression is closely associated with EBV+ and MSI-H GC, PD-L1 may also be expressed through adaptive immune resistance, which occurs due to the many cytotoxic T-cells and neoantigens present within tumor cells (secondary to EBV itself and the many frameshift mutations seen in EBV+ and MSI-H cancers) and is associated with favorable prognosis. These contradictory results suggest that PD-L1 expression in GC is caused either by oncogenic stimulation resulting in poor prognosis and by adaptive immune resistance affecting favorable prognosis bringing favorable prognosis, and those results are consistent with previous observations in melanoma¹⁸.

Classifying GC based on PD-L1 expression and TIL may be more complex than the initial morphological studies performed in melanoma using IHC analyses suggest, and will likely require quantitative and special determination to be used as highly predictive tools to define optimal therapy for patients with advanced cancers¹¹. In the present study, we performed PD-L1 IHC with SP142, an FDA-approved antibody, in whole sections of 241 surgically resected GCs. The cases included many EBV+ (N = 40) and MSI-H (N = 76) GCs, and the study measured PD-L1 with QIA to assess its clinical significance and possible utility in pathology. In our previous study on TME classified by manual interpretation of PD-L1 and CD8 using the same IHC-stained slides, type I (PD-L1^H and CD8^H) showed the best survival and was enriched with EBV+ and MSI-H GC cases. The classification of TME groups in The Cancer Genome Atlas (TCGA) data based on PD-L1 and TIL status, the type I TME was associated with oncogenic viral infection¹⁹. In the present study, we found similar results to these TCGA results and our previous analyses: EBV+ GC cases are mostly type I TME, while MSI-H GC cases are somewhat scattered,

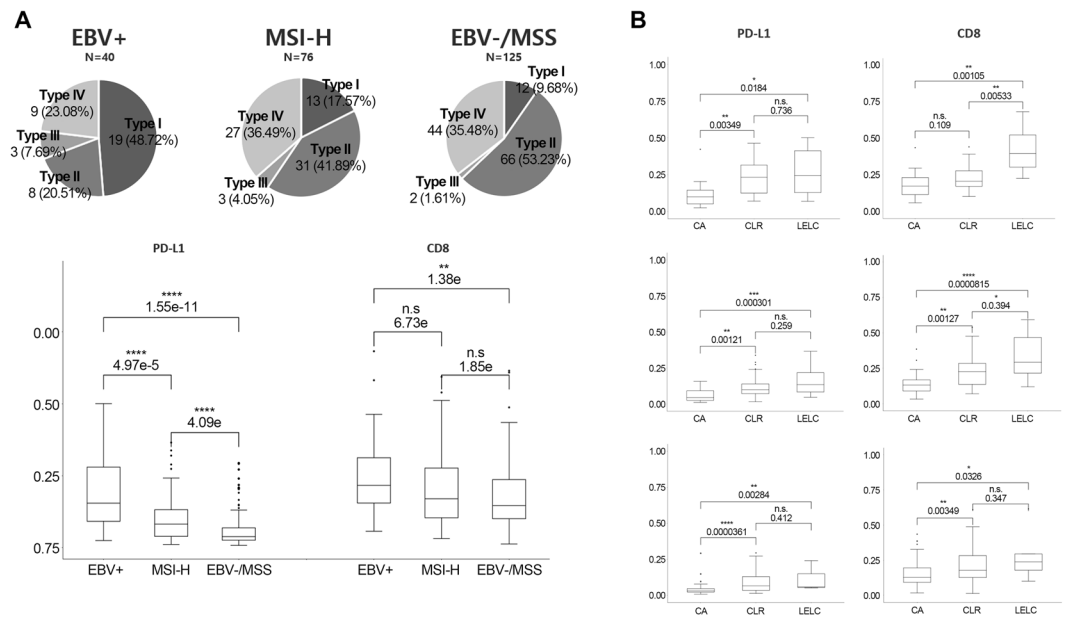


Figure 5. (A) Pie charts of TME subtypes based on PD-L1 and CD8 quantitative image analyses (upper) and PD-L1/CD8 ratio in each subtype of gastric cancer (lower). (B) PD-L1 and CD8 ratio in relation to host inflammatory responses in EBV+ (upper), MSI-H (middle) and EBV-/MSS gastric cancers.

with a diversity of TME subtypes¹⁹. Various expression patterns of PD-L1 and their prognostic significance have also been reported^{20,21}. We recently found that all EBV+ GCs with PD-L1 expression responded dramatically to pembrolizumab; however, not all MSI-H GCs express PD-L1, and only patients with PD-L1-expressing GC responded well to pembrolizumab. PD-L1 expression was the most useful of the predictive markers used in that study²².

In this study, we introduced QIA to interpret the IHC results of PD-L1 and CD8, and the results were directly compared with manual interpretation results and mRNA expression levels. Given that manual interpretation has limitations, such as low reproducibility and high inter-observer variation, analysis by QIA can reduce inter-observer variation, provide more objective and unbiased assessments, and improve the reproducibility of interpretation. Moreover, it can facilitate the collection of large amounts of data for statistical analysis and increase the efficiency of pathological interpretation by assessing numerous samples in a short time. In the present study, QIA of IHC-stained, whole-slide images correlated very well with microscopic interpretation of PD-L1 and mRNA levels. Moreover, the CD8 ratio significantly correlated with CD8 mRNA levels. Our results highlight the positive aspects of QIA for digital images. Future work should focus on deep assessment of IHC-stained images with integrated regional information.

Although this study was the first to analyze PD-L1 and CD8 expression status by QIA in a large cohort of GC cases, it has some limitations. First, selection bias is possible because this is a retrospective study, and no patients were treated with immunotherapy. Second, although SP142 is an FDA-approved antibody, this clone was developed for atezolizumab biomarker assays for urothelial carcinoma and non-small cell lung cancers⁸. To overcome these limitations, we are planning future stratification studies on GC patients with known responses to immunotherapy.

In conclusion, QIA correlated well with mRNA levels and the manual interpretation results of IHC. We successfully classified four TME groups of GC based on the QIA results of whole digitalized slide images for PD-L1 and CD8 expression status. These results demonstrate that QIA can be used as a diagnostic tool to classify TME subtype.

Material and Methods

Patient selection. Patients who underwent surgery for primary gastric carcinoma from September 2004 to May 2012 at the Samsung Medical Center were eligible for this study. Among them, 40 EBV+ positive cases, 76 MSI-H cases, and 125 EBV(-)/MSS cases were selected, for a total of 241 patients with GC, as previously described¹². No patient had received preoperative chemotherapy and/or radiation therapy or had any other uncontrolled cancer at the time of GC diagnosis. The mean follow-up period was 48.4 ± 20.1 months. Four patients developed other organ cancers (lung, skin, pancreas, and colon) during the follow-up period. Clinical data, including demographic features, pathological characteristics, and treatment outcomes, were obtained by reviewing medical records, and information on deaths was provided by the national statistical office. Tumor stage was defined according to TNM classification as described in the 8th edition of the AJCC cancer staging manual²³. Informed consent was obtained from all patients and the Institutional Review Board of the Samsung Medical Center approved this study. This study was carried out in accordance with the approved guidelines.

Immunohistochemistry and quantitative image analysis. IHC was performed on each representative whole section from all 241 formalin-fixed paraffin-embedded (FFPE) GC samples. Staining for PD-L1 was conducted using a Food and Drug Administration (FDA)-approved rabbit anti-human PD-L1 monoclonal antibody (clone SP142; Ventana, Tucson, AZ, USA). The percentages of tumor cells and peritumoral immune cells that stained positive for PD-L1 (combined positive score: CPS) were analyzed independently by two pathologists (J.C. and K.M.K.). Staining for CD8 in FFPE tissue sections was conducted using a CONFIRM-anti-CD8 (SP57) rabbit monoclonal primary antibody without dilution with Ventana BenchMark XT via the OptiView DAB IHC Detection Kit (Catalog Number 760–700; Ventana).

All IHC-stained slides were digitally scanned at 20x magnification using a ScanScope Aperio AT Turbo slide scanner (Leica Microsystems). The computational whole slide digital image workflow encompasses three steps: (1) image preprocessing, (2) nuclei segmentation, and (3) quantitative image analysis. In image preprocessing, a color deconvolution technique²⁴ was used to separate the pure DAB and hematoxylin-stained areas, leaving a complementary image. Hematoxylin-stained images were then used for cell segmentation based on our segmentation algorithm²⁵. The chromogenic intensity in DAB-stained images was then quantified (i.e., for PD-L1 and CD8). In the quantitative image analysis, single cell-based information, including pixel intensity and cell size measurements (i.e., pixel area), was visualized using a bivariate scatter plot (Fig. 1 shows an example). In addition, the chromogenic signal intensity was quantitatively measured, which is analogous to the fluorescence-activated cell sorting data obtained in flow cytometry²⁶. Thresholds for cell type identification (i.e., positive/negative) were determined based on the distribution of scatter plots, and the same value was used across all samples. The PD-L1/CD8 positive cell ratio was defined as the absolute number of positive cells per total number of cells.

PD-L1 and CD8 mRNA analysis. Total RNA extracted from the available GC FFPE specimens was used to measure PD-L1 and CD8 gene expression with nCounter[®] Gene Expression Human Immunology Panel containing 494 human immune signature genes (NanoString Technologies, Seattle, WA, USA). For all selected cases, archival tissue was available for RNA extraction, with an estimated tumor cell percentage over 60% after dissection under microscopy. Total RNA (200 ng) was extracted from three to four 4- μ m-thick tissue sections of representative primary tumor blocks using a High Pure RNA Paraffin kit (Roche Diagnostic, Mannheim, Germany). RNAs were hybridized to target sequence-specific capture probes and fluorescent-labeled reporter probes. The mRNA-probe complexes were washed, immobilized, and quantified by fluorescence imaging as previously described^{27,28}, and part of the results were published previously²⁹.

Statistical analysis. The clinicopathological characteristics of patients, such as age, sex, pTNM stage (AJCC 7th edition), disease-free survival (DFS), and overall survival (OS), were analyzed. The SPSS 18.0 statistical software program (SPSS Inc., Chicago, IL, USA) was used for statistical analyses. PD-L1 expression status, CD8 expression status, and clinicopathological variables were compared using Pearson's chi-squared test, and the results were further compared using a linear-by-linear association. The mean values of PD-L1 ratio and CD8 ratio were compared using a Kruskal-Wallis test. The Kaplan-Meier method was used to estimate DFS and OS. To evaluate the associations between clinicopathological factors and survival, a Cox proportional hazard model was used. P-values less than 0.05 were considered statistically significant.

References

- Gavrieliades, M. A., Gallas, B. D., Lenz, P., Badano, A. & Hewitt, S. M. Observer variability in the interpretation of HER2/neu immunohistochemical expression with unaided and computer-aided digital microscopy. *Arch Pathol Lab Med* **135**, 233–242 (2011).
- Aeffner, F. *et al.* The Gold Standard Paradox in Digital Image Analysis: Manual Versus Automated Scoring as Ground Truth. *Arch Pathol Lab Med* **141**, 1267–1275 (2017).
- Guillaud, M. *et al.* Subvisual chromatin changes in cervical epithelium measured by texture image analysis and correlated with HPV. *Gynecol Oncol* **99**, S16–23 (2005).
- Chen, F. *et al.* New horizons in tumor microenvironment biology: challenges and opportunities. *BMC Med* **13**, 45 (2015).
- Parra, E. R. *et al.* Image Analysis-based Assessment of PD-L1 and Tumor-Associated Immune Cells Density Supports Distinct Intratumoral Microenvironment Groups in Non-small Cell Lung Carcinoma Patients. *Clin Cancer Res* **22**, 6278–6289 (2016).
- Kawazoe, A. *et al.* Clinicopathological features of programmed death ligand 1 expression with tumor-infiltrating lymphocyte, mismatch repair, and Epstein-Barr virus status in a large cohort of gastric cancer patients. *Gastric Cancer* **20**, 407–415 (2017).
- Koh, J. *et al.* Clinicopathologic implications of immune classification by PD-L1 expression and CD8-positive tumor-infiltrating lymphocytes in stage II and III gastric cancer patients. *Oncotarget* **8**, 26356–26367 (2017).
- Kerr, K. M. & Hirsch, F. R. Programmed Death Ligand-1 Immunohistochemistry: Friend or Foe? *Arch Pathol Lab Med* **140**, 326–331 (2016).
- Abozeid, M., Rosato, A. & Sommaggio, R. Immunotherapeutic Strategies for Gastric Carcinoma: A Review of Preclinical and Clinical Recent Development. *Biomed Res Int* **2017**, 5791262 (2017).
- T. H. Maxstat: Maximally selected rank statistics. *R package version 0*, 7–21 (2015).
- Teng, M. W., Ngiew, S. F., Ribas, A. & Smyth, M. J. Classifying Cancers Based on T-cell Infiltration and PD-L1. *Cancer Res* **75**, 2139–2145 (2015).
- Cho, J. *et al.* Four distinct immune microenvironment subtypes in gastric adenocarcinoma with special reference to microsatellite instability. *ESMO Open* **3** (2018).
- Romano, E. & Romero, P. The therapeutic promise of disrupting the PD-1/PD-L1 immune checkpoint in cancer: unleashing the CD8 T cell mediated anti-tumor activity results in significant, unprecedented clinical efficacy in various solid tumors. *J Immunother Cancer* **3**, 15 (2015).
- Raufi, A. G. & Klempner, S. J. Immunotherapy for advanced gastric and esophageal cancer: preclinical rationale and ongoing clinical investigations. *J Gastrointest Oncol* **6**, 561–569 (2015).
- Lee, K. S. *et al.* Prognostic implication of CD274 (PD-L1) protein expression in tumor-infiltrating immune cells for microsatellite unstable and stable colorectal cancer. *Cancer Immunol Immunother* (2017).
- Derks, S. *et al.* Abundant PD-L1 expression in Epstein-Barr Virus-infected gastric cancers. *Oncotarget* **7**, 32925–32932 (2016).
- Gu, L. *et al.* PD-L1 and gastric cancer prognosis: A systematic review and meta-analysis. *PLoS One* **12**, e0182692 (2017).
- Taube, J. M. *et al.* Colocalization of inflammatory response with B7-h1 expression in human melanocytic lesions supports an adaptive resistance mechanism of immune escape. *Sci Transl Med* **4**, 127ra137 (2012).

19. Ock, C. Y. *et al.* Pan-Cancer Immunogenomic Perspective on the Tumor Microenvironment Based on PD-L1 and CD8 T-Cell Infiltration. *Clin Cancer Res* **22**, 2261–2270 (2016).
20. Cho, J. *et al.* Programmed cell death-ligand 1 expression predicts survival in patients with gastric carcinoma with microsatellite instability. *Oncotarget* **8**, 13320–13328 (2017).
21. Cho, J. *et al.* Four distinct immune microenvironment subtypes in gastric adenocarcinoma with special reference to microsatellite instability. *ESMO Open* **3**, e000326 (2018).
22. Kim, S. T. *et al.* Comprehensive molecular characterization of clinical responses to PD-1 inhibition in metastatic gastric cancer. *Nat Med* (2018).
23. *AJCC Cancer Staging Manual*. 7 edn, (Springer-Verlag New York, 2010).
24. Ruifrok, A. C., Katz, R. L. & Johnston, D. A. Comparison of quantification of histochemical staining by hue-saturation-intensity (HSI) transformation and color-deconvolution. *Appl Immunohistochem Mol Morphol* **11**, 85–91 (2003).
25. Chang, Y. H. *et al.* Quantitative analysis of histological tissue image based on cytological profiles and spatial statistics. *Conf Proc IEEE Eng Med Biol Soc* **2016**, 1175–1178 (2016).
26. Tsujikawa, T. *et al.* Quantitative Multiplex Immunohistochemistry Reveals Myeloid-Inflamed Tumor-Immune Complexity Associated with Poor Prognosis. *Cell Rep* **19**, 203–217 (2017).
27. Lee, J. *et al.* Nanostring-based multigene assay to predict recurrence for gastric cancer patients after surgery. *PLoS One* **9**, e90133 (2014).
28. Lin, S. J. *et al.* Signatures of tumour immunity distinguish Asian and non-Asian gastric adenocarcinomas. *Gut* (2014).
29. Park, C. *et al.* Host immune response index in gastric cancer identified by comprehensive analyses of tumor immunity. *Oncoimmunology* **6**, e1356150 (2017).

Acknowledgements

This research was supported by a grant (H16C1990 from the Korean Health Technology R&D Project, Ministry of Health & Welfare). Y.H.C. acknowledges grant support by the AACR SU2C (SU2C-AACR-DT12-14), the NCI U54CA209988, the Brenden-Colson Center for Pancreatic Care and the OHSU Center for Spatial Systems Biomedicine (OCSSB).

Author Contributions

Y.H.C. and Y.J.H. conducted and analyzed the digital image analyses and computational measurements; J.C. and J.L. analyzed the clinical and pathological features. J.L., S.Y.S. and K.M.K. designed the experimental requirements; Y.H.C., Y.J.H., J.C. and K.M.K. wrote the manuscript. All authors critically revised the manuscript and provided intellectual content.

Additional Information

Supplementary information accompanies this paper at <https://doi.org/10.1038/s41598-018-32299-0>.

Competing Interests: The authors declare no competing interests.

Publisher's note: Springer Nature remains neutral with regard to jurisdictional claims in published maps and institutional affiliations.



Open Access This article is licensed under a Creative Commons Attribution 4.0 International License, which permits use, sharing, adaptation, distribution and reproduction in any medium or format, as long as you give appropriate credit to the original author(s) and the source, provide a link to the Creative Commons license, and indicate if changes were made. The images or other third party material in this article are included in the article's Creative Commons license, unless indicated otherwise in a credit line to the material. If material is not included in the article's Creative Commons license and your intended use is not permitted by statutory regulation or exceeds the permitted use, you will need to obtain permission directly from the copyright holder. To view a copy of this license, visit <http://creativecommons.org/licenses/by/4.0/>.

© The Author(s) 2018